Metasurface Antennas for FMCW Radar

Modeste Bodehou, *Member, IEEE*, Gilles Monnoyer, *Graduate Student Member, IEEE*, Maxime Drouguet, Khaldoun Al Khalifeh, *Member, IEEE*, Luc Vandendorpe, *Fellow, IEEE*, and Christophe Craeye, *Senior Member, IEEE*

***Abstract*—Two planar metasurface (MTS) antennas are designed to produce a pattern with optimal illumination in a radar scenario, given the a priori known path of the targets. The antennas are extremely flat, thin, with a monopole feed integrated in the plane of the structure. The monopole serves as a surface-wave (SW) launcher illuminating the slab. The excited SW progressively leaks after interacting with the MTS, forming a radiation pattern designed to cover uniformly a portion of road in a given scenario. The realized antennas radiation patterns are experimentally validated. The MTSs are then deployed in a frequency-modulated continuous wave radar system. The experiments showed that the echo of the targets in the range-Doppler map does not statistically depend on the distance between the target and the radar, while a clear range dependence is observed when classical patch array antennas are used. That means, given the capability to engineer a particular shape for the radiation pattern and the interest for simultaneously detecting small and big targets, the MTS antennas allow one to better resolve a small and distant target, next to a big and close one.**

***Index Terms*—Beam shaping, FMCW radar, metasurfaces.**

I. Introduction

FREQUENCY modulated continuous wave (FMCW) radars are very convenient for range and velocity detection, at short to medium distances. They also have a clear advantage over infrared and optical sensors at night and in bad atmospheric conditions [1]. FMCW radars are increasingly realized with antenna arrays [2]. While arrays can be designed to provide high gain, their complexity as well as the power losses may significantly increase when a proper control of the radiated field over the space is required. Metasurfaces (MTSs) provide an efficient and low-cost alternative for the manipulation of radiated fields [4]. MTSs acting in reflection or transmission have been proposed in the literature for radar antennas [3]. MTSs can also be engineered to transform surface-waves (SW) into leaky-waves (LW) [5]–[7]. In the latter case, the antenna is particularly low profile and it also includes the feeder, as preferred in many radar configurations. SW-based MTS antennas usually comprise a dense array of subwavelength patches printed on a grounded slab. The antenna is fed by a SW launcher (a pin) and the patches act as a sheet impedance. The latter is defined as the ratio between the electric field and the averaged equivalent current flowing on the MTS [8]. Spatially modulating the surface impedance enables the transformation of the SW into LW, in a controlled way (see Fig. 1). The first synthesis methods for such antennas were based on holography and have enabled the generation of pencil beams through the control of the phase of the aperture field [9]. Amplitude and phase synthesis of the aperture field has been proposed in [10] for locally sinusoidal modulation, and further developed in [11] for monopulse radar with broadside pencil beam radiation. Very recently, an electric field integral-equation based direct synthesis method has been proposed [12]–[14]. Rather than solving the integral equation to compute the surface current distribution flowing on a known MTS (traditionally the case for analysis), the MTS is here assumed unknown, and is derived from an estimate of the surface current. The latter is related to the desired radiation pattern. This novel synthesis method is particularly useful to generate complex-shaped radiation patterns as demonstrated in [7]. In surveillance applications, where it is required to simultaneously have a wide field of view, having a high gain is not sufficient. In that case, the shaped antenna pattern should compensate the effect of the free-space path loss due to varying distance, while focusing the radiated power in the area of interest. The goal of this letter is twofold. First, further experimental validations of the integral equation method is provided for a shaped-beam MTS antenna adapted to radar applications. Second, the MTSs are incorporated into an FMCW radar system and the impact of the MTS antennas on the observed range-Doppler diagram is discussed. In particular, it is shown that the usage of the MTS antennas improves the probability of detection of a small and distant target in the vicinity of a bigger and close target. The letter is structured as follows. Section II briefly recalls the MTS synthesis method. Section III provides a general description of the used radar system, and Section IV is devoted to numerical and experimental results.

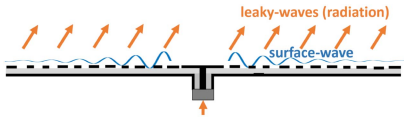

Fig. 1. MTS antenna illustration.

II. MTS Antennas Analysis and Design

The sheet impedance $\underline{\underline{\mathbf{Z}}}_S$ relates the averaged (homogenized) surface current $\mathbf{J}$ flowing on the MTS to the averaged tangential

Manuscript received 19 September 2022; revised 15 November 2022; accepted 13 December 2022. Date of publication 27 December 2022; date of current version 5 May 2023. This work was supported in part by the Belgian FNRS Chargé de Recherches program and in part by the Belgian Aspirant FNRS grant. *(Corresponding author: Modeste Bodehou.)*

The authors are with the ICTEAM Institute, Université catholique de Louvain, 1348 Louvain-la-Neuve, Belgium (e-mail: modeste.bodehou@uclouvain.be; gilles.monnoyer@uclouvain.be; maxime.drouguet@uclouvain.be; khaldoun.alkhalifeh@uclouvain.be; luc.vandendorpe@uclouvain.be; christophe.craeye@uclouvain.be).

Digital Object Identifier 10.1109/LAWP.2022.3231683

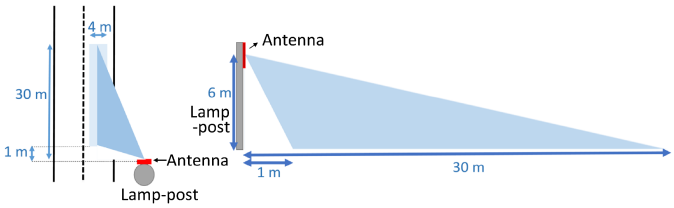

Fig. 2. Configuration of radar on a lamp-post next to the road. The light-blue area represents the coverage zone, focused along the right lane. Left: top view. Right: side view.

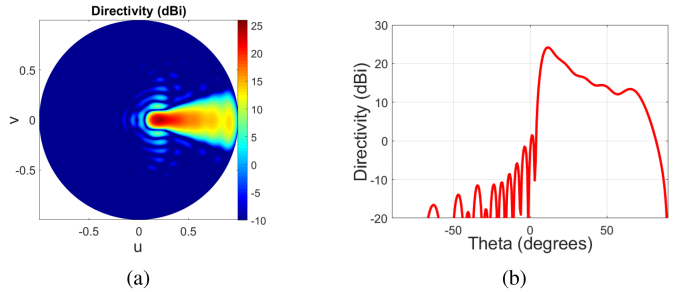

(a) (b)

Fig. 3. Desired radiation pattern. (a) Illustration in the *uv* plane. (b) Cut of the radiation pattern in the plane $\phi = 0$.

(a) (b)

Fig. 4. Illustration of the FMCW radar system. (a) Front view: antennas part. (b) Back view: system part. The top left green board is the transmitter (BGT24MTR11 from Infineon [25]) connected either to the Tx serial patch antenna or to the Tx MTS antenna. A copy of the Tx signal is used as the local oscillator for the dual receiver (BGT24MR2 from Infineon [26]) and its associated baseband amplifiers and filters on the bottom right board. The Rx serial patch antenna and the Rx MTS antenna are both connected to the dual receiver to ease the comparison. The generation of the calibrated signal used to tune the integrated oscillator for the frequency modulation, and the data acquisition are performed by a PicoScope 3404D from Pico Technology [27].

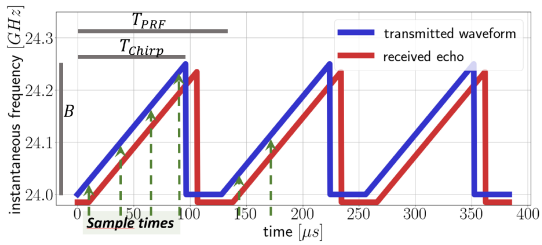

Fig. 5. Representation of the modulation of a linear chirp FMCW radar. The received signal is a frequency-shifted and delayed version of the transmitted one due to the Doppler effect and the distance travelled by the wave.

electric field $\mathbf{E}_t$ at the MTS. The surface current therefore satisfies the following integral equation [8]:

$$\hat{\mathbf{z}} \times \left[\iint_{S'} \underline{\underline{\mathbf{G}}}^{EJ}(\boldsymbol{\rho}, \boldsymbol{\rho}') \, \mathbf{J}(\boldsymbol{\rho}') \, dS' - \underline{\underline{\mathbf{Z}}}_S(\boldsymbol{\rho}) \, \mathbf{J}(\boldsymbol{\rho}) \right] = -\hat{\mathbf{z}} \times \mathbf{E}_i \tag{1}$$

where $\hat{\mathbf{z}}$ is the normal to the surface, $\underline{\underline{\mathbf{G}}}^{EJ}$ is the dyadic Green's function providing the electric field generated at $\boldsymbol{\rho}$ by a point-source current placed at $\boldsymbol{\rho}'$, and $\mathbf{E}_i$ is the excitation electric field. In an analysis problem, (1) is solved to provide the current $\mathbf{J}$ consistent with a given surface impedance $\underline{\underline{\mathbf{Z}}}_S$ and a given excitation $\mathbf{E}_i$. This is done with the Method of Moments (MoM) by expanding the surface current into a set of basis functions, followed by a testing of the fields with the same basis functions (Galerkin testing). In this sense, Gaussian ring basis functions (GRBF) [15] and Fourier–Bessel basis functions (FBBF) [16] have been proposed in the literature to compactly represent the current distribution for MTSs designed on circular or possibly elliptical apertures. Efficient methods capable of analyzing arbitrarily shaped MTSs have recently been proposed in [17].

When designing MTS antennas, the unknown is the surface impedance $\underline{\underline{\mathbf{Z}}}_S$, which is assumed to be modulated around a known average $\underline{\underline{\mathbf{Z}}}_0$. The considered surface impedance is capacitive and anisotropic, so as to support the propagation of dominantly transverse magnetic (TM) SWs. The desired visible spectrum of the current distribution can be derived from the desired radiation pattern. As shown in [12], the surface impedance can be computed with the MoM, assuming a given current distribution $\mathbf{J}$ and excitation electric field $\mathbf{E}_i$. The invisible current distribution being a priori unknown, it is guessed from the one consistent with the average impedance. The estimated current distribution $\mathbf{J}$ is used to derive the required lossless surface impedance. The modulation depth is then optimized to find a good compromise between the aperture efficiency and the conversion efficiency of the antenna. The conversion efficiency is defined as the ratio between the power radiated by the antenna, assuming an infinite slab, and the feeding power [18]. The conversion efficiency should be as high as possible to avoid undesired diffraction effects at the antenna rim.

In this letter, the two antennas (one on the transmit side, Tx, and the other on the receive side, Rx) are designed to cover with uniform power a road in a scenario represented in Fig. 2.

The desired radiation pattern, considering the limited size of the antenna, is shown in Fig. 3. The pattern then looks like a cosecant squared diagram [19] in elevation. The only difference between the two antennas is in their polarization. The first antenna is right-handed circularly polarized, while the second one is left-handed circularly polarized so as to take into account the change in polarization after reflection by a smooth perfect electric conductor.

III. FMCW Radar System and Signal

We consider a continuous-wave radar with a linear chirp modulation of frequency. This type of radar is widely used for traffic control because the observation range is limited and the hardware is cheap [23], [24]. The system is schematically represented in Fig. 4.

The radar sends chirp signals of duration $T_{PRF} = 128\,\mu s$, with PRF referring to the pulse repetition frequency. During each pulse (chirp), the frequency is linearly modulated as shown in Fig. 5.

The emitted chirp signal can be written as

$$s(t) = Ae^{\mathrm{j}(2\pi(f_0 t + \frac{B}{T_{Chirp}}\frac{t^2}{2})+\varphi)} \tag{2}$$

where A is the amplitude of the signal, φ is an arbitrary phase constant, $f_0 = 23.75$ GHz is the minimum frequency, $B = 250$ MHz is the modulation bandwidth, and $T_{Chirp} = 96\,\mu s$ the actual duration of the linear chirp excluding necessary breaks between chirps, as shown in Fig 5. After scattering by the target, the signal is received by the radar as represented in red in Fig. 5. The received signal is then mixed with the emitted one, resulting in a baseband signal whose frequency is related to the distance and to the velocity of the target. This baseband signal is sampled and the samples corresponding to pauses between chirps are discarded. Considering K targets, N chirps, a sampling period T_s with M samples per chirp, the acquired baseband signal can be written, in good approximation, as a $M \times N$ matrix whose elements are given as follows [18], [20], [21]:

$$y_{m,n} = \sum_{k=1}^{K} \alpha_k e^{-\mathrm{j}2\pi(\mu_k m + \nu_k n)} + \text{Noise} \tag{3}$$

where $\mu_k = (2BT_s/c)r_k$, and $\nu_k = (2f_0 T_{PRF}/c)v_k$, with c being the speed of light; r_k, the distance to the target; v_k, the velocity of the kth target. Finally, α_k is a complex variable that takes into account all attenuation and phase shift between the transmitted and received signals. The modulus of α_k is related to the power of the emitted signal through the radar equation [28]

$$|\alpha_k|^2 \propto \frac{\lambda^2 A^2 \sigma_k}{(4\pi)^3 r_k^4} G^2 \tag{4}$$

where G is the antenna gain in the direction of the target; $\lambda = c/f_0$ is the wavelength of operation; σ_k is the radar cross section of the target. In practice, it is difficult to predict the value of σ_k because the target has a nonpredictable shape and orientation. Therefore, α_k is usually assumed randomly distributed with parameters that can be, for instance, roughly estimated from measurements [29].

Once the baseband matrix $y_{m,n}$ is acquired, the range-Doppler diagram can be derived through a 2-D Fourier transform. It is worth mentioning that since the Fourier transform is carried out on a finite duration, each target on the range-Doppler diagram will appear as a 2-D sinc function U_k centered at r_k, v_k, with a main lobe width proportional to $(c/2B)$ (range resolution) in the range direction, and proportional to $\lambda/(2NT_{PRF})$ (speed resolution) in the speed direction. Although complex algorithms for multiple target parameters estimation have been proposed in the literature [29], [30], [31], it is reasonable to consider in a very general scenario that a target can be detected if the peak level given by $|\alpha_k|$ of a considered target is significantly higher than the secondary lobes (or main lobe) level generated by other observed targets at the considered target position, as illustrated in Fig. 6. Another condition is that $|\alpha_k|$ should be above the noise level.

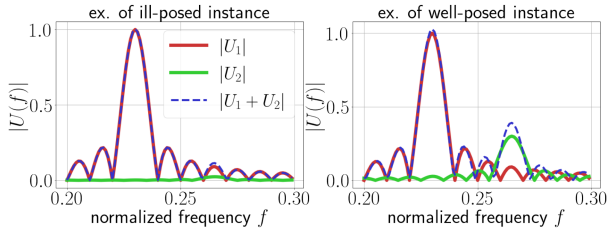

Fig. 6. 1-D slice of the Fourier transform of an ill-posed (left) and a well-posed (right) signal ($N = 1$ and $K = 2$). The Fourier transform of the noiseless signal resulting from the observation of the two targets is given by the dashed line $|U_1 + U_2|$. Because algorithms rely on finding peaks in this function, the estimation of the weaker target on the example on the left is likely to fail.

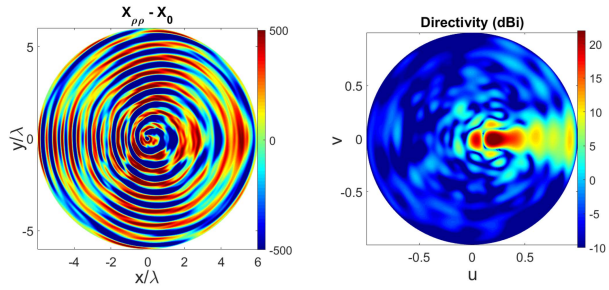

Fig. 7. Synthesis results. (a) $\rho\rho$ component of the reactance modulation. ρ and ϕ are the polar coordinates. (b) Directivity of the effectively implemented surface impedance, in the *uv* plane.

IV. Results

A. MTS Antennas

This section presents the design results of the MTS antennas based on the synthesis method proposed in [7] and [12]. The antennas are designed to operate at 24 GHz, with a substrate of relative permittivity $\epsilon_r = 3.66$, and thickness $d = 1.524$ mm. The average reactance (imaginary part of the average impedance) is $X_0 = -804\,\Omega$. Both antennas are circular with a radius equal to $6\,\lambda$, with λ being the free-space wavelength at 24 GHz. The synthesized surface impedance of the first antenna is represented in Fig. 7. The modulation depth has been optimized to find a good compromise between the aperture efficiency and the conversion efficiency, given the limited aperture size and the single monopole feeder [7], [14]. The surface impedance is implemented with the coffee-bean patches proposed in [5], using the procedure described in [7]. The resulting radiation pattern, considering the effectively implemented surface impedance is computed with the MoM code based on full-domain basis functions [16], and is represented in Fig. 7(b). The measured radiation patterns in the plane $\phi = 0$ for the two antennas are reported in Fig. 8. The measurements have been carried out between 23.7 and 24 GHz because the RF signal is modulated within that frequency band. It can be observed that the shape of the pattern is preserved in the frequency band of interest. The measured gain is 22 dBi, which compares well with the ideal gain (24 dBi). The difference can be explained by the inaccuracy of the surface impedance implementation with printed patches, and by diffraction at the substrate rim [14].

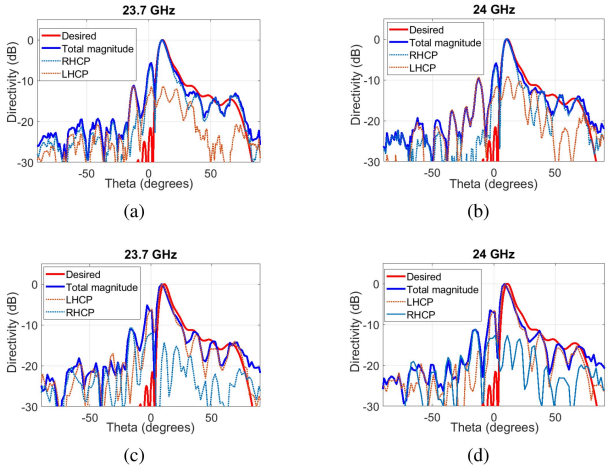

Fig. 8. Measured radiation pattern. (a) and (b) First antenna at 23.7 and 24 GHz. (c) and (d) Second antenna at 23.7 and 24 GHz.

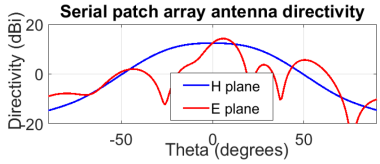

Fig. 9. Directivity of the serial patch antenna array simulated with the CST commercial software [32].

B. Patch Array Antenna

For qualitative analysis purposes, classical serial patch array antennas are considered, as shown in Fig. 4(a). The surface of each patch array antenna is 18 cm^2. This type of antennas is used in commercial FMCW radar systems. The simulated radiation pattern in the E- and H-plane is represented in Fig. 9. The directivity of the patch array is 14 dBi.

C. FMCW Radar Measurement

In this section, the performance of the FMCW radar is analyzed in two different cases. In the first case, the MTS antennas are used for both Rx and Tx, and in the second case, the serial patch antenna array has been adopted [see Fig. 4(a)]. In both cases, we have used the same emitted power. For a fair comparison, the serial patch antenna array has been disposed horizontally and tilted, so that its main beam points in the same direction as that of the MTS antenna. In this way, the patch array will cover the road as well as possible.

The measurements have been made during three minutes to observe several targets. The received signal has been analyzed as described in Section III to extract the range-Doppler map. Fig. 10 illustrates the properties of the observed targets. Each point in the graph represents a couple $(|\alpha_k|^2,\ r_k)$ estimated from the range-Doppler map.

As expected, in both cases, the amplitude of the targets are randomly distributed. However, two observations can be made. First, $|\alpha|$ is higher when the MTSs are used. This observation can be attributed to the smaller size of the serial patch array antenna, which provides a lower gain than the MTS (14 vs 22 dBi). Second, on the average, and in the sector of interest (distance ranging from 10 to 30 m), $|\alpha|$ is almost constant with respect to the distance in the MTS case, while it significantly decreases with the distance when the serial patch array antenna is adopted. The latter observation is due to the particular shape of the radiation pattern of the MTS antenna, and this implies that the probability to simultaneously detect a distant and/or small target (low RCS) in the vicinity of a closer and/or larger target is higher when the MTS antennas are used. In other words, as explained by Fig. 6, the response from the weaker target is no longer hidden by the sidelobes of the response of the stronger target. This aspect is illustrated in Fig. 11.

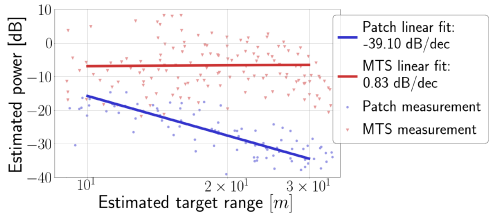

Fig. 10. Range-Power diagram comparing the estimated power from observation of cars with the FMCW radar when using either the MTS antennas or regular serial patch array antennas. Dots results from one *frame* composed of $N \times M$ samples acquired from the baseband signal. Solid lines: logscale linear fitting of the dots.

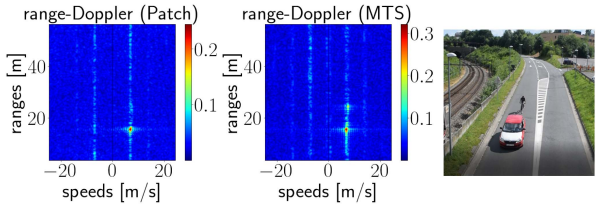

Fig. 11. Example of range-Doppler maps from 2-D Fourier transform of signals from a single measurement performed simultaneously with the serial patch array antennas (left) and with the MTS antennas (center). Observation of two targets as shown on the photograph on the right. The two targets appear distinguishably in the MTS antennas scenario while the weaker one (a bike) is hidden by the stronger target (a car) when patch array antennas are used.

V. Conclusion

Two MTS antennas with opposite polarizations have been designed for an FMCW radar system devoted to traffic control applications. The MTSs have been designed to cover uniformly a road in a specific scenario, in the frequency band of the commercial FMCW radar systems operating at 24 GHz. It has been shown that the usage of MTSs specifically designed to cover an a priori known path significantly improves the detection probability of a small and/or distant target, in the presence of a strong and/or close one. Given the possibility to generate very complex radiation patterns with MTSs [7], it becomes possible to homogeneously illuminate complex, possibly sinuous, paths.

References

[1] E. Tavanti et al., "A short-range FMCW radar-based approach for multi-target human-vehicle detection," *IEEE Trans. Geosci. Remote Sens.*, vol. 60, 2022, Art. no. 2003816.

[2] A. Ganis et al., "A portable 3-D imaging FMCW MIMO radar demonstrator with a 24 × 24 antenna array for medium-range applications," *IEEE Trans. Geosci. Remote Sens.*, vol. 56, no. 1, pp. 298–312, Jan. 2018.
[3] K. V. Mishra et al., "Reconfigurable metasurfaces for radar and communications systems," URSI AP-RASC, Mar. 2019.
[4] O. Quevedo-Teruel et al., "Roadmap on metasurfaces," *J. Opt.*, vol. 21, pp. 1–44, Jul. 2019.
[5] G. Minatti et al., "Modulated metasurface antennas for space: Synthesis, analysis and realizations," *IEEE Trans. Antennas Propag.*, vol. 63, no. 4, pp. 1288–1300, Apr. 2015.
[6] M. Faenzi et al., "Metasurface antennas: New models, applications and realizations," *Sci. Rep.*, vol. 9, pp. 1–14, 2019.
[7] M. Bodehou, K. Alkhalifeh, S. N. Jha, and C. Craeye, "Direct numerical inversion methods for the design of surface-wave based metasurface antennas: Fundamentals, realization, and perspectives," *IEEE Antennas Propag. Mag.*, vol. 64, no. 4, pp. 24–36, Aug. 2022.
[8] M. A. Francavilla, E. Martini, S. Maci, and G. Vecchi, "On the numerical simulation of metasurfaces with impedance boundary condition integral equations," *IEEE Trans. Antennas Propag.*, vol. 63, no. 5, pp. 2153–2161, May 2015.
[9] B. H. Fong, J. S. Colbrun, J. J. Ottusch, J. L. Visher, and D. F. Sievenpiper, "Scalar and tensor holographic artificial impedance surfaces," *IEEE Trans. Antennas Propag.*, vol. 58, no. 10, pp. 3212–3221, Oct. 2010.
[10] G. Minatti, F. Caminita, E. Martini, M. Sabbadini, and S. Maci, "Synthesis of modulated-metasurface antennas with amplitude, phase, and polarization control," *IEEE Trans. Antennas Propag.*, vol. 64, no. 9, pp. 3907–3919, Sep. 2016.
[11] M. Faenzi et al., "A metasurface radar monopulse antenna," *IEEE Trans. Antennas Propag.*, vol. 70, no. 4, pp. 2571–2579, Apr. 2022.
[12] M. Bodehou, C. Craeye, E. Martini, and I. Huynen, "A quasi-direct method for the surface impedance design of modulated metasurface antennas," *IEEE Trans. Antennas Propag.*, vol. 67, no. 1, pp. 24–36, Jan. 2019.
[13] M. Bodehou, E. Martini, S. Maci, I. Huynen, and C. Craeye, "Multibeam and beam scanning with modulated metasurfaces," *IEEE Trans. Antennas Propag.*, vol. 68, no. 3, pp. 1273–1281, Mar. 2020.
[14] M. Bodehou and C. Craeye, "Array surface-wave launcher for the efficient generation of shaped beam and multibeam with metasurface," *IEEE Trans. Antennas Propag.*, vol. 69, no. 12, pp. 8860–8865, Dec. 2021.
[15] D. González-Ovejero and S. Maci, "Gaussian ring basis functions for the analysis of modulated metasurface antennas," *IEEE Trans. Antennas Propag.*, vol. 63, no. 9, pp. 3982–3993, Sep. 2015.
[16] M. Bodehou, D. González-Ovejero, C. Craeye, and I. Huynen, "Method of moments simulation of modulated metasurface antennas with a set of orthogonal entire-domain basis functions," *IEEE Trans. Antennas Propag.*, vol. 67, no. 2, pp. 1119–1130, Feb. 2019.
[17] J. Cavillot, M. Bodehou, S. Hubert, and C. Craeye, "Efficient analysis of planar, arbitrarily shaped, and (bi)-anisotropic metasurface antennas," *IEEE Trans. Antennas Propag.*, vol. 70, no. 1, pp. 536–546, Jan. 2022.
[18] M. Bodehou, D. González-Ovejero, C. Craeye, S. Maci, I. Huynen, and E. Martini, "Power balance and efficiency of metasurface antennas," *Sci. Rep.*, vol. 7, pp. 1–11, 2020.
[19] G. Carluccio, A. Mazzinghi, and A. Freni, "Design and manufacture of cosecant-squared complementary reflect arrays for low-cost applications," *IEEE Trans. Antennas Propag.*, vol. 65, no. 10, pp. 5220–5227, Oct. 2017.
[20] T. Feuillen, A. Mallat, and L. Vandendorpe, "Stepped frequency radar for automotive application: Range-doppler coupling and distortions analysis," in *Proc. 2016 IEEE Mil. Commun. Conf. (MILCOM)*, 2016, pp. 894–899.
[21] Y. Liu, H. Meng, G. Li, and X. Wang, "Velocity estimation and range shift compensation for high range resolution profiling in stepped-frequency radar," *IEEE Geosc. Remote Sens. Lett.*, vol. 7, no. 4, pp. 791–795, Oct. 2010.
[22] H. Bao, "The research of velocity compensation method based on range-profile function," *Int. J. Hybrid Inf. Technol.*, vol. 7, pp. 49–56, 2014.
[23] S. Saponara and B. Neri, "Radar sensor signal acquisition and 3 d FFT processing for smart mobility surveillance systems," in *Proc. IEEE Sensors Appli. Symp.*, 2016, pp. 1–6.
[24] J.-J. Lin, Y.-P. Li, W.-C. Hsu, and T.-S. Lee, "Design of an FMCW radar baseband signal processing system for automotive application," *SpringerPlus*, 2016.
[25] BGT24MTR11. [Online]. Available: https://www.infineon.com/cms/en/product/sensor/radar-sensors/radar-sensors-for-iot/24ghz-radar/bgt24mtr11/
[26] BGT24MR2. [Online]. Available: https://www.infineon.com/cms/en/product/sensor/radar-sensors/radar-sensors-for-iot/24ghz-radar/bgt24mr2/
[27] 3404D PicoScope. [Online]. Available: https://www.picotech.com/download/datasheets/PicoScope3000DDMSOSeriesDataSheet-fr.pdf
[28] J. R. Probert-Jones, "The radar equation in meteorology," *Quart. J. Roy. Meteorol. Soc.*, vol. 88, pp. 485–495, 1962.
[29] S. M. Patole, M. Torlak, D. Wang, and M. Ali, "Automotive radars: A review of signal processing techniques," *IEEE Signal Process. Mag.*, vol. 34, no. 2, pp. 22–35, Mar. 2017.
[30] L. Zheng and X. Wang, "Super-resolution delay-Doppler estimation for OFDM passive radar," *IEEE Trans. Signal Process.*, vol. 65, no. 9, pp. 2197–2210, May 2017.
[31] G. M. de Galland, T. Feuillen, L. Vandendorpe, and L. Jacques, "Sparse factorization-based detection of off-the-grid moving targets using FMCW radars," in *Proc. IEEE Int. Conf. Acoust., Speech Signal Process.*, 2021, pp. 4575–4579.
[32] Computer Simulation Technology (CST). [Online]. Available: https://www.3ds.com/fr/produits-et-services/simulia/produits/cst-studio-suite/